Progress In Electromagnetics Research B, Vol. 97, 149–166, 2022

Systematic Design & Analysis of a 42 GHz Gyrotron and the Effects of Structure & Beam Parameters on Its RF Performance

Ashutosh Singh[1, *] and Pradeep K. Jain[2]

Abstract—The systematic design approach of a 42 GHz CW gyrotron has been extensively presented in this paper. Beam-wave interaction of the conventional tapered cylindrical cavity gyrotron is demonstrated using commercially available Particle-In-Cell (PIC) code. Beam absent and beam present cases have been considered to observe the performance of the device. Beam absent case is presented to validate the design in desired mode as well as resonant frequency whereas beam present case is demonstrated to validate and observe the beam-wave interaction behavior of the device in terms of output power. In order to optimize the dimension of interaction structure to achieve desired performance of the device, several parameters were considered. RF output power of the device is estimated with the variation of structure parameters as well as electron beam parameters to achieve better performance in terms of efficiency. Using the designed parameters, beam present analysis offers a saturated output power well above 250 kW. The particles phase space behavior along the interaction length is demonstrated to realize the energy transfer phenomena. The PIC simulation results are found in close agreement with the self-consistent single-mode results. The estimated output power and efficiency support the proper design of proposed gyrotron oscillator.

1. INTRODUCTION

Gyrotron oscillators have proven their usefulness as considerable efficient and reliable radiation sources capable of delivering the higher power ranging from hundred kilowatts to several megawatts in the microwave, millimeter, and sub-millimeter wavelength [1]. The conventional microwave vacuum electronic devices like klystrons, TWTs, magnetrons, etc. are not capable to produce the higher power comparatively in the millimeter and sub-millimeter wavelength region due to various inherent technical limitations [2]. Gyrotron surpasses these conventional microwave vacuum amplifiers or oscillators in terms of both power and efficiency. Presently, the high power generation attribute is the main thrust to the research and development of the gyrotron in both pulse and continuous operation [1]. Gyrotrons find a variety of scientific, medical, strategic, communication, and industrial applications due to its wide range of power level. Gyrotrons producing moderate level of power in millimeter to sub-millimeter wave have applications as in high resolution radars ranging and imaging in atmospheric and planetary science, ceramic sintering, plasma scattering measurements, electron spin resonance (ESR) experiments, and nuclear magnetic resonance (NMR) signal enhancement by dynamic nuclear polarization (DNP), etc. [1–6]. However, the high power gyrotrons at high frequency are playing important role in the area of plasma fusion research. Powerful gyrotrons, providing more than MW power level, are mainly used for electron cyclotron resonance plasma heating (ECRH) in both tokamaks and stellarators, controlling of local current density profile by non-inductive electron cyclotron current drive (ECCD), stability control

Received 14 September 2022, Accepted 22 November 2022, Scheduled 4 December 2022

* Corresponding author: Ashutosh Singh (asingh.rs.ece@iitbhu.ac.in).

[1] Department of Physics, Mahesh Prasad Sinha Science College, Babasaheb Bhimrao Ambedkar Bihar University, Muzaffarpur 842001, India. [2] Department of Electronics and Communication Engineering, National Institute of Technology Patna, Patna, Bihar 800005, India.

and diagnostics of magnetically confined plasmas for generation of energy by controlled thermonuclear fusion [1–6].

Gyrotrons are fast wave vacuum electron tubes whose operation is based on electron cyclotron resonance maser (ECRM) instability by involving the interaction between RF electromagnetic wave and space charge cyclotron wave on the annular gyrating electron beam in a smooth wall interaction structure supporting a fast waveguide mode. The gyrotron consists of several components like electron beam source (magnetron injection gun (MIG)), beam tunnel, a tapered cylindrical RF interaction cavity surrounded by a superconducting magnet, quasi-optical launcher, collector, RF window, magnet system, etc. (Fig. 1(a)). MIG produces annular gyrating electron beam. The axial velocity (v_z) enables the electron beam to convey along the cavity, and the transverse velocity ($v_\perp$) makes the electrons interact with the transverse component of RF electric field for RF power growth. The electron beam gyrates in the background of static magnetic field produced by a superconducting magnet, and its interaction with RF causes azimuthal phase bunching of the electrons. The choice of magnetic field is kept in such a way that the cyclotron frequency in fundamental or harmonics is close to the frequency of RF field. The interaction structure of a gyrotron contains mainly three sections, i.e., down taper, straight cylindrical section, and up taper (Fig. 1(b)). In the down taper section, the cross sectional area of the waveguide is decreased gradually towards the gun end. This down tapering is done to attain a cutoff for the RF wave that prevents from the back propagation of RF towards the gun side. The second section, middle portion, of the RF cavity is the uniform cylindrical cross section where RF fields attain the maximum value. The output taper is the up-taper section of the cavity, and this facilitates the conversion of the standing RF wave into the travelling wave to couple it out from the cavity structure. During the beam-wave interaction, there is a net energy transfer from electron beam to RF with the condition that the RF frequency is slightly larger than the relativistic electron cyclotron frequency or one of its harmonics. After this energy transfer, spent electron beam is collected on the collector of uniform output waveguide section. The grown RF signal is extracted through an RF window which also provides a vacuum seal for the tube [7]. In the case of radial extraction, the RF output power is converted into a Gaussian beam by using a mode converter before extraction through the ceramic window. Apart from these,

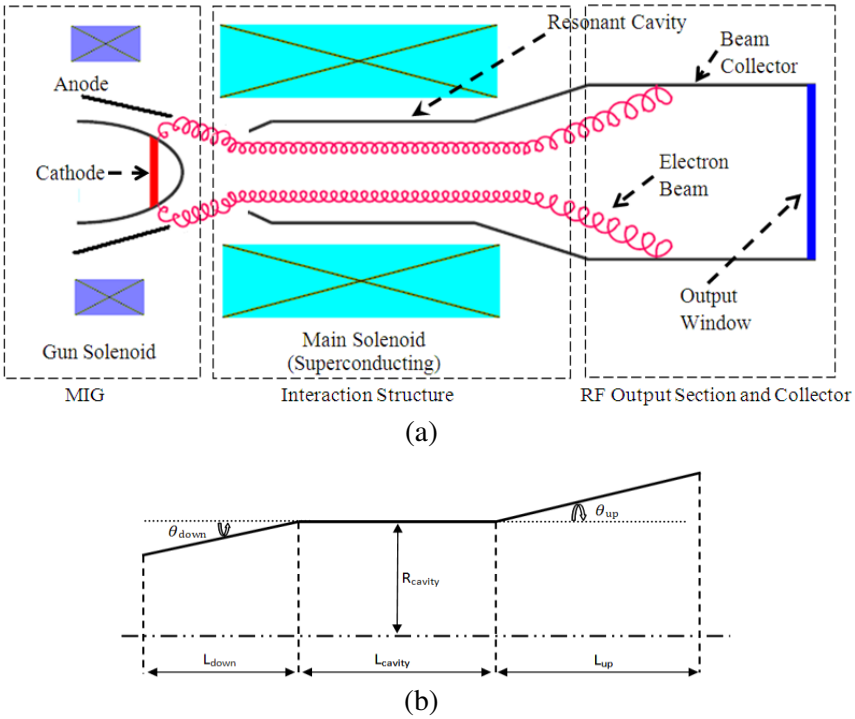

Figure 1. (a) Schematic arrangement of a gyrotron oscillator and (b) design of a tapered cavity interaction structure.

operating in the higher order modes property of the gyrotron appreciably alleviates the problem of wall heating and beam interception in comparison to other microwave devices. Additionally, the harmonic operation of gyrotron reduces the high magnetic field requirement in comparison to fundamental mode of operation [8].

A large number of literatures have been published to demonstrate the mathematical model for the design and analysis of the gyrotron using linear and nonlinear approaches [8, 9]. On the other hand, with the advent of fast computers, Particle-In-Cell (PIC) simulation offers more insight in understanding as well as supporting the stabilized theories. Presently, PIC codes are widely used by the researchers to investigate the RF behavior of the gyro-devices and also helpful to improve the design of the device [5, 10–13]. Several works have been reported in the literature in the past about the design and analysis of 42 GHz gyrotron. Singh et al. have presented the design of 42 GHz, 200 kW Gyrotron using in-house developed codes and commercially available software [12]. They have presented the design of a triode type MIG, cavity geometry, and selection of the operating mode. The cavity was cold analyzed as well as with beam present, and an output power above 200 kW has been obtained at the guiding magnetic field 1.60 T–1.65 T [12]. Kartikeyan et al. have also presented 42 GHz CW gyrotron delivering excess of 200 kW output power with efficiency of $\sim 38\%$ for plasma heating in a small experimental tokamak using single-mode analysis and time-dependent self-consistent (SELFT) computations [13].

The present work is a detailed investigation of the design and analysis of a 42 GHz, 200 kW gyrotron oscillator systematically and its beam-wave interaction mechanism in a tapered cylindrical interaction structure using a commercially available PIC tool MAGIC [14]. Here, it is intended to demonstrate fully nonlinear behavior of the interaction mechanism in terms of saturation and efficiency of output radiation. The beam absent and present cases are considered for the investigation of RF behavior of interaction structure. Beam absent case is performed to ensure the device operation in the desired mode and frequency whereas the beam present case is presented to examine the device performance in order to generate the desired RF power output. All the particles are monitored throughout the interaction length to have information about beam quality in terms of spreading or dispersion. The field value is recorded in time domain, and its Fourier transform provides the frequency operation of the device. Electron beamlets are observed to realize the bunching mechanism and the RF field pattern to ensure the device operation in the desired mode. The energy of all the particles along the interaction length is observed to realize the energy transfer characteristics which can also be understood by the total positive power of particles along the axis of cavity. The output power growth is also observed at the output end cross section of the interaction structure. This provides the information of the device stability and saturated output power level. The output power is calculated by varying the various dependencies such as beam energy, beam current, beam velocity ratio α, and applied DC magnetic field with the mid-section length as a parameter. The sensitivity of output power with these dependencies is discussed. These results of output power are compared with the those obtained through the self-consistent single-mode (SSM) analysis.

Table 1. Design goal of the gyrotron.

Particulars	**Specifications**
Mode	TE_{03}
Frequency	42 ± 0.05 GHz
Accelerating voltage (V_b)	60–70 kV
Beam current (I_b)	8–12 A
Velocity ratio (α)	1.3–1.5
Magnetic field (B_0)	1.6–1.62 T
Output power (P_{out})	≈ 200 kW
Efficiency (η)	$\sim 35\%$
Estimated Wall loading	$< 2.0\,\mathrm{kW/cm^2}$
Diffractive (Q_D)	$\approx$ 800–900

2. DESIGN APPROACH OF A 42 GHZ GYROTRON

The interaction structure is a crucial component in a gyrotron responsible for amplifying the RF. The selection of interaction structure geometry should be chosen in such a way that the efficiency of the energy exchange from the electron beam to RF wave is as high as possible with desired RF mode excitation. Additionally, the electron beam parameters should be estimated properly to ensure the excitation of desired operating mode which interacts with electron beam to generate RF output of desired level. The design of gyrotron oscillator is discussed in this section with the design goal as given in Table 1 and the cavity dimension listed in Table 2.

Table 2. Structure parameter of tapered cavity.

Parameters	Value
L_{down}	30 mm
L_{cavity}	44 mm
L_{up}	46 mm
θ_{down}	2°
θ_{cavity}	0°
θ_{up}	3°

2.1. Mode Selection

The gyrotron should oscillate at the specific frequency in the specific mode for efficient power output. The device operation in the parasitic modes results in shift in its oscillation frequency and also a decrease in the efficiency. In order to ensure the design mode excitation, various factors have to be considered. Generally, the mode, for which the self-excitation conditions are first satisfied during the start-up, is established inside the interaction structure. This happens because the mode, which starts growing first, is likely to suppress other competing modes. Therefore, proper design of the device ensures the desired mode operation instead of other parasitic competing modes. For the operation in TE_{mn} mode, the cavity wall radius (r_w) is related to λ by $r_w = (v_{mn}\lambda/2\pi)$, where v_{mn} is the nth root of derivative of Bessel function $(J'_m(x)) = 0$. The optimum electron beam radius is given by $r_b = (v_{m\pm s,\,i} r_w/v_{mn}) = (v_{m\pm s,\,i}\lambda/2\pi)$ ($i = 1$ or 2), where s is the harmonic number. In general, the co-rotating mode (with the lower sign) is chosen since this provides better coupling of the electron beam to the RF field [13].

2.2. Coupling Coefficient and Start Oscillation Current

The coupling coefficient offers the choice of optimised electron beam radius to have maximum coupling for the design mode [13]. The second radial maximum of TE_{03} mode at 0.52 normalized beam radius is the position for maximum coupling (Fig. 2(a)). A gyrotron will not oscillate if the beam current is below the threshold value, i.e., start oscillation current (I_{start}), which depends on beam properties, magnetic field, resonator geometry, etc. From Fig. 2(b), it can be observed that for the required TE_{03} operating mode, beam current can be taken as 10 A for the 1.61 T magnetic field. There are two important mode competitors, TE_{23} and TE_{52}, which might couple to electron beam and start oscillating. The proper selection of beam parameters would restrict the oscillation of unwanted modes.

2.3. Ohmic Loss/Wall Loss Consideration

Ohmic loss is one of the major constraints in the gyrotron operation. The expression of Ohmic loss density can be expressed in terms of the normalized parameters F (normalized field amplitude), μ (normalized interaction length), and Δ (detuning parameter) as [15]

$$\rho_{\text{ohm}}\,(\text{W/m}^2) = 5.1 \times 10^{-15}\sigma^{-0.5}\omega^{2.5}F^2\beta_t^6 C_t^2\gamma^2(1 - 0.5\beta_t^2\Delta)^2 \tag{1}$$

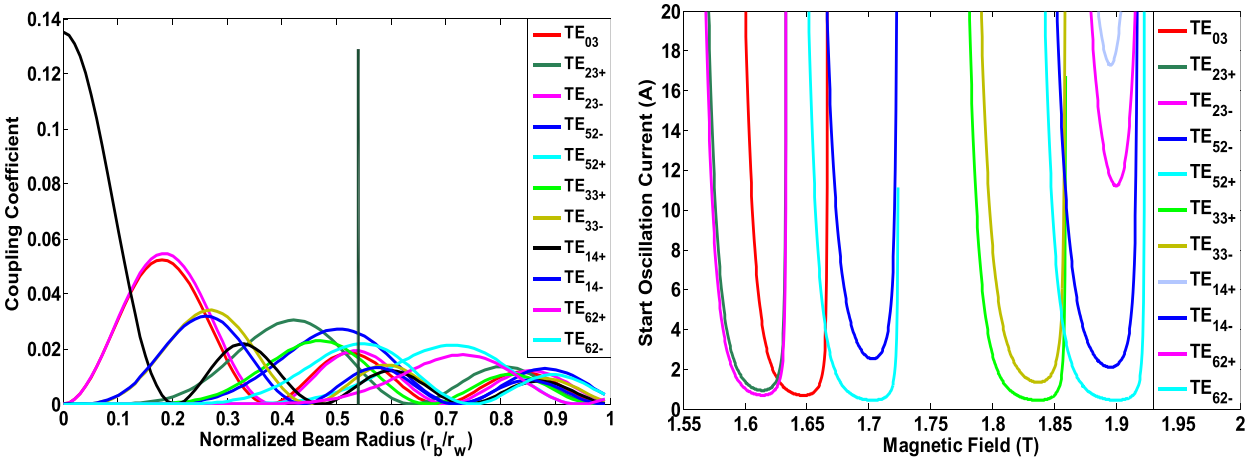

Figure 2. (a) Coupling coefficient with respect to the normalized beam radius (vertical line shows the position of electron beam coupled to second maximum of TE_{03} mode). (b) Start oscillation current as a function of magnetic field.

where $C_t = J_m(v_{mn})/J_{m\pm s}(k_{mn}r_b)$, σ is the electrical conductivity of the cavity wall, β_t the transverse phase velocity, and γ the relativistic mass factor. This will provide the choice of the cathode voltage and field amplitude for a tolerable wall loss. The diffractive Q_D of gyrotron cavities, which leads to the power extracted from the end of the resonator, is [13, 15] $Q_D = \frac{4\pi}{1-R_{out}}\left(\frac{L}{\lambda}\right)^2$, where L is the length parameter of the effective Gaussian field profile $f(z) = \exp(-4z^2/L^2)$; R_{out} is the reflectivity at the output end of the cavity; at the input end it is assumed to be 1 due to the cutoff condition for the operating mode. Equation relating the cavity mode indices to the Ohmic loss density for given output power is as [15]

$$\left(\nu_{mn}^2 - m^2\right) = \frac{16\pi}{c^3}\sqrt{\frac{2}{\sigma\mu_0}}\left(\frac{L}{\lambda}\right)\frac{Pf^{5/2}}{(1-R_{out})\rho_{\text{ohm}}} = 1.05\times10^{-3}\left(\frac{L}{\lambda}\right)\frac{P\,(\text{MW})f^{5/2}\,(\text{GHz})}{(1-R_{out})\rho_{\text{ohm}}\,(\text{kW/cm}^2)} \tag{2}$$

This equation shows a trade-off between power and frequency for the same operating mode. The maximum wall loss with mode eigenvalue can be estimated from the equation [7]

$$\left(\frac{dP}{dA}\right)_{\max} \approx \sqrt{\frac{8}{\pi}}\sqrt{\frac{1}{\pi Z_0\sigma}}\frac{PQ}{L\lambda^{1.5}}\frac{1}{(\nu_{mn}^2 - m^2)} \tag{3}$$

where $Z_0 = 377\,\Omega$ is the impedance of the free space. For the finite field amplitude, the beam voltage can be estimated for a particular wall loss density from Fig. 3(a). For a particular beam voltage, loss increases with raising the RF field amplitude. Hence, the choice of the maximum field amplitude is restricted due to wall loss. Fig. 3(b) shows the trade-off between mode eigenvalue and the wall loss with the maximum output power as a parameter. For TE_{03} mode of operation and 200 kW of output power, wall loss corresponds to less than $3\,\text{kW/cm}^2$.

2.4. Equicontour Curve of Oscillation Frequency

The contour plot of oscillation frequency with respect to beam current and magnetic field is shown in Fig. 4. The equicontour plot of frequency is used to optimize the beam parameters. For a fixed value of magnetic field and beam current, the oscillation frequency can be chosen. From this figure, one can observe the increase in oscillation frequency with the increase in both beam current and magnetic field.

2.5. Voltage Depression and Limiting Current

Voltage depression is one of the limiting factors in the high power gyrotrons [13, 15]. It affects the resonance condition as well as beam pitch factor. Additionally, it increases the velocity spread which

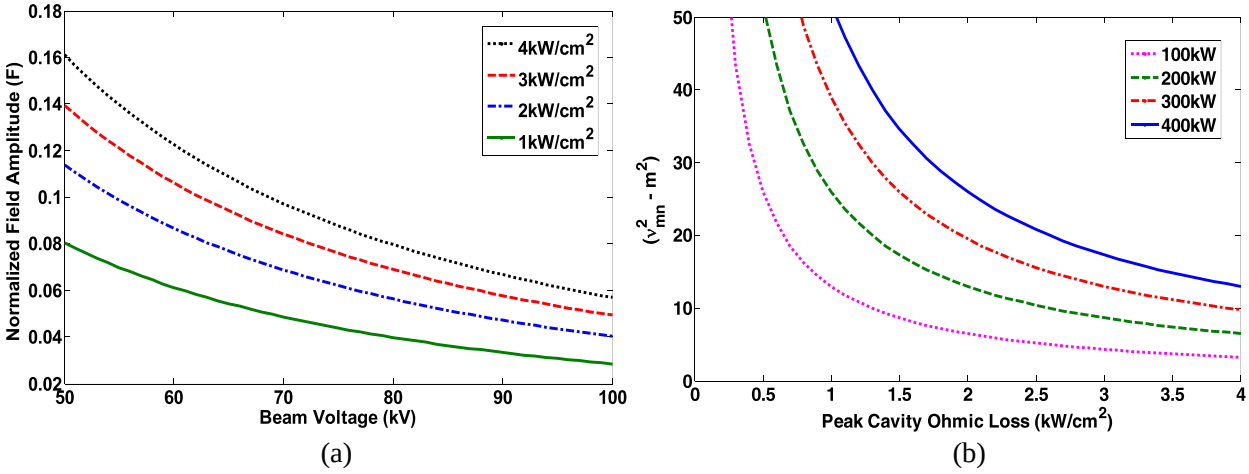

Figure 3. (a) Normalized field amplitude versus cathode voltage with cavity wall Ohmic heating density as a parameter and (b) cavity mode indices versus Ohmic power loss density with output power as a parameter for the 42 GHz gyrotron.

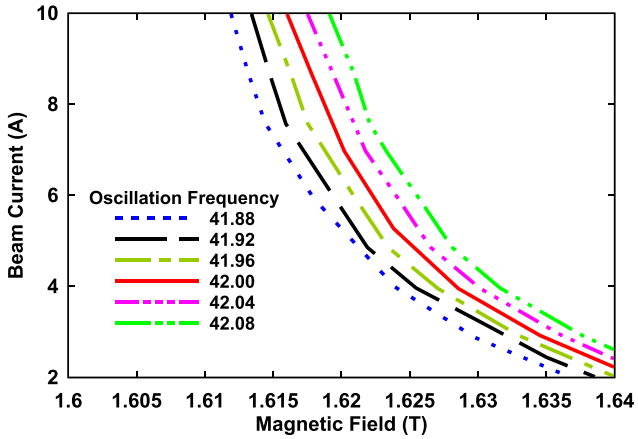

Figure 4. Oscillation frequency equicontour curve as a function of magnetic field (B_0) versus beam current (I_b).

results in poor beam quality as well as the reduction in efficiency. In a cylindrical cavity with radius (r_w), the potential depression (V_{dep}) between the cavity wall and the axis of symmetry due to a concentric electron beam with a uniform current density is given by [13, 15]

$$V_{dep} \approx 60 \frac{I_b}{\beta_z} \ln\left(\frac{r_w}{r_b}\right), \tag{4}$$

As a consequence of the voltage depression, a limiting current (I_L) can be determined for a given momentum and cathode voltage. The increase in current beyond I_L causes the voltage depression enhancement in such a way that the axial velocity is reduced to zero, and beam no longer propagates and is reflected back. For thin electron beam, limiting current is written as

$$\frac{I_L}{8500} \approx I^* / \ln\left(\frac{r_w}{r_b}\right) \tag{5}$$

where,

$$I^* = \gamma_0 \left[1 - \left(1 - \beta_{z0}^2\right)^{1/3}\right]^{3/2} \tag{6}$$

Table 3. Characteristics of different modes.

m	n	ν_{mn}	r_w (mm)	r_b (mm)	V_{dep} (kW)	I_L (A)	dP/dA (kW/cm^2)
0	2	7.015588	7.98	2.09	2.99	29.1	0.104
*0	2	7.015588	7.98	6.05	0.51	138.1	0.104
0	3	10.173469	11.57	2.09	3.82	22.8	0.049
*0	3	10.173469	11.57	6.06	1.44	59.0	0.049
2	1	3.054232	3.47	2.09	1.13	76.9	0.958
2	2	6.706135	7.62	2.09	2.89	30.1	0.125
2	3	9.969469	11.33	2.09	2.89	30.1	0.054
*2	3	9.969469	11.33	6.06	1.40	61.0	0.054
4	2	9.282396	10.55	4.78	1.77	49.1	0.073
5	2	10.519861	11.96	6.05	1.53	57.0	0.060

(For the modes marked with '*', the electron beam is positioned at the 2nd radial maximum of the RF field).

In Table 3, the various parameters for the possible operating modes are listed. The most important competing modes operating around the same frequency with the more or less same beam radius are TE_{23} (41.16 GHz) and TE_{52} (43.43 GHz). Since the voltage depression is much higher ($\approx$ 3 kV) if the beam is placed at the first radial maximum of the fields, the beam is placed at the second radial maximum. Therefore, one can operate at either of these modes without changing the electron gun. As far as the wall loading is concerned, both these modes tend to operate well within the limitation. But for the TE_{52} voltage depression is very high, so TE_{03} is selected for the design purpose. Apart from this, the choice of mode becomes important because of the stored energy factor ($\nu_{mn}^2 - m^2$). For a given value of ν_{mn}, symmetric modes with $m = 0$ have the most stored energy, while whispering-gallery modes with $\nu_{mn} \sim m$ have the least [15]. Consequently, TE_{03} mode is chosen preferably over the others.

3. PARTICLE-IN-CELL (PIC) SIMULATION DESCRIPTION

Particle-In-Cell (PIC) is a technique commonly used to simulate the motion of charged particles in the presence of electromagnetic wave by solving the Maxwell equations together with the Lorentz particle motion equation for all discrete mesh points in the space and in the series of discrete time steps. PIC codes offer the realization of behavior of the device without actual fabrication in order to save time and expenses. The complete optimization for desired performance of the device can be achieved using PIC codes. Here, a user configurable PIC simulation code based on finite-difference time-domain method (FDTD) method called 'MAGIC' is used for the modeling of the device and simulation of beam-wave interaction and electro-energetic processes between space charge and RF fields. MAGIC code is well suited to investigate the beam-wave interaction phenomena, and it provides self consistent interaction between charged particles and electromagnetic fields [14]. MAGIC involves several basic steps for any problem as the selection of coordinate systems, grids, represent/generate structural geometries, outer boundaries, material properties, incoming and outgoing wave, particle emission processes, output, ion motion, and other phenomena. In the simulation of tapered interaction structure of gyrotron, a code has been developed for 3D structure of cavity. This structure is simulated using MAGIC3D solver with different spatial commands of desired dimension and proper coordinate system. The structure is then discretized which is an important step to control the accuracy of the results in simulation, and it must fulfill the Courant criteria to have a convergent solution. The number of grid cells controls the accuracy of solution as well as simulation time. Further, the field algorithm command MAXWELL is assigned which solves Maxwell's equations to obtain electromagnetic fields in time and space. Next, EMISSION command is used to specify the emission properties to the cathode surface,

and EMIT command enables emission from the specific object surface. A gyro-magnetic electron beam is introduced at down taper end of the confining interaction structure to introduce the oscillations inside using EMISSION GYRO command with assigning the value of beam current, static magnetic field, axial and transverse momentum, and guiding center radius. The gyro emission produces a beam center axis parallel to the externally applied magnetic field. Depending on the structure geometry, RF in the desired mode is set up from the noise background in the cavity, and it starts amplify. Appropriate boundary conditions for the cavity are applied, and external DC magnetic field is applied using PRESET command. OBSERVE command is used to observe the various fields components and power. PHASESPACE command provides the trajectory of the particles in phase space. All the processes can be controlled using TIMER command which enables investigation of the particular information at any time instant.

4. RF BEHAVIOR

The tapered cylindrical cavity structure is simulated in both beam absent and beam present cases. Beam absent simulation is performed to ensure the desired mode of operation at specific resonant frequency and to estimate the resonant frequency, field patterns, and Ohmic quality factor of the desired mode. Beam present case illustrates the complete beam-wave interaction behavior. For both cases, the 3D structure model used in simulation is shown in Fig. 5.

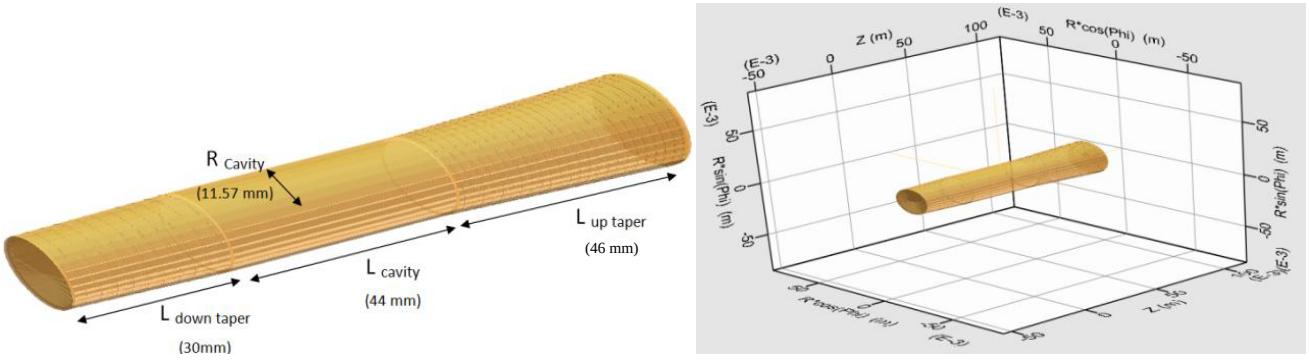

Figure 5. Three-dimensional view of tapered circular interaction structure used in simulation.

4.1. Beam Absent Simulation and Parametric Analysis

The cold cavity simulation is performed using EIGENMODE command which specifies an eigenvalue solution of the fully time-dependent Maxwell's equations. The field patterns on different planes of interest as well as field profile along the radial and axial positions are observed to ensure the desired mode. The electric and magnetic field patterns in the mid plane of cylindrical section are shown in Figs. 6(a) & 6(b). Clearly, the vector plot of electric and magnetic fields ensures TE_{03} mode at 42 GHz

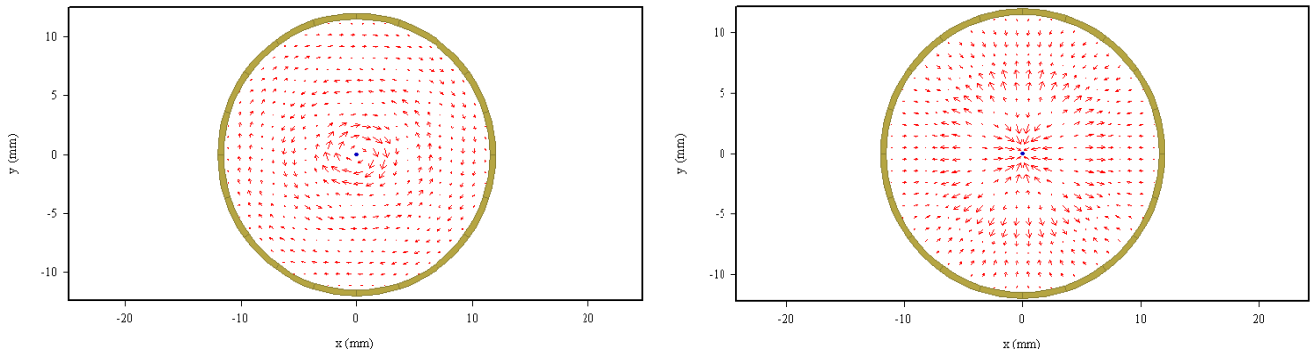

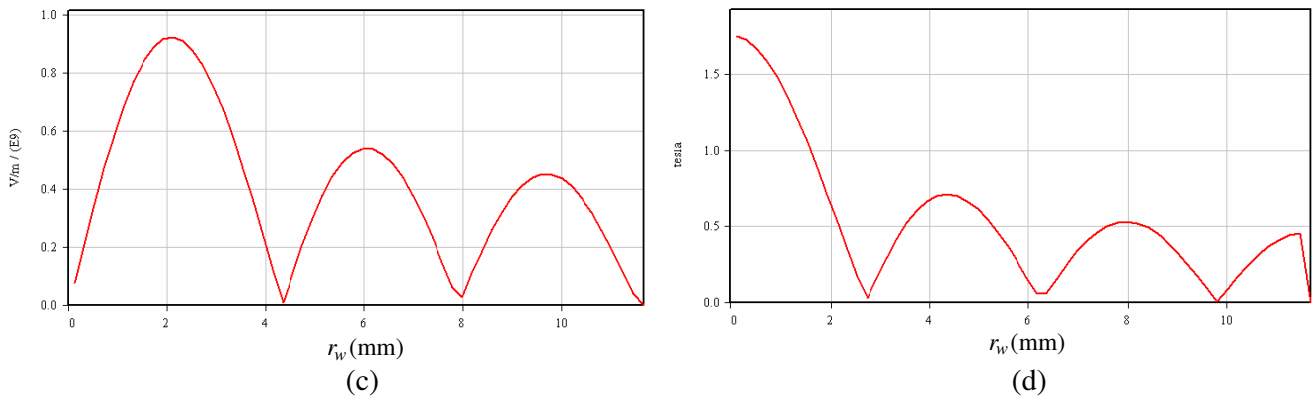

Figure 6. Vector plot of absolute field profiles at the cylindrical mid-plane of a tapered cavity interaction structure, (a) electric field and (b) magnetic field. Radial variation of absolute field values, (c) electric field, (d) magnetic field.

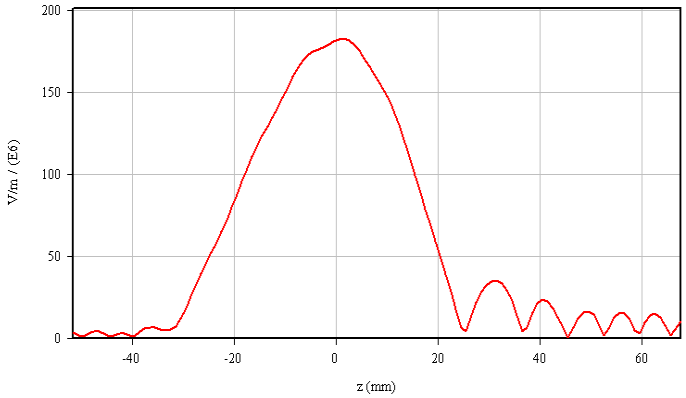

Figure 7. Variation of absolute electric field magnitude along axial direction of tapered cavity.

resonant frequency with magnitude as well as orientation. The variations of electric and magnetic field magnitudes along the cavity radius (r_w) are shown in Figs. 6(c) & 6(d). In Fig. 7, the absolute electric field along the axis of the interaction structure is the maximum in cylindrical region. It strongly decays in input taper region and almost vanishes towards down-taper end whereas it is oscillatory in output taper region with reduced amplitude as compared to the cylindrical section.

Parametric variation is performed in this section to realize the dependency of the device performance on it. In the device operation, it is always taken care of that device must operate at desired frequency with good quality factor. The power content should be the maximum in desired mode in comparison to other competing modes. Resonant frequency is mainly influenced by the structure parameters, so sensitivity analysis has been performed to see the influence of structure parameters on the resonant frequency and Ohmic quality factor.

4.1.1. Variation of Midsection Length

The resonant frequency and quality factor decrease with the increase of the length of the cavity midsection (Fig. 8). At the length of 44 mm, the frequency is exactly 42 GHz, i.e., desirable resonant frequency. Henceforth, the mid section length should be around 44 mm to keep desired resonant frequency.

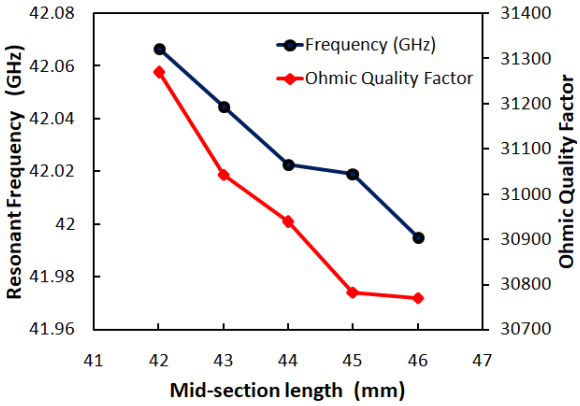

Figure 8. Resonant frequency and Ohmic quality factor variation with cylindrical midsection length, ($L_{\text{down}} = 30\,\text{mm}$, $L_{\text{up}} = 46\,\text{mm}$, $\theta_{\text{down}} = 2°$, $\theta_{\text{up}} = 3°$).

4.1.2. Variation of Taper Angles

The resonant frequency and quality factor decrease with the increase in the down taper angle (Fig. 9(a)). At an angle of 1 to 3 degrees, the resonant frequency is close to the resonant frequency of the cavity. From Fig. 9, it is understood that the variation of resonant frequency is small, i.e., very less dependent on the taper angle. The Ohmic quality factor increases with increasing the output taper angle on the contrary to varying down taper angle (Fig. 9(b)).

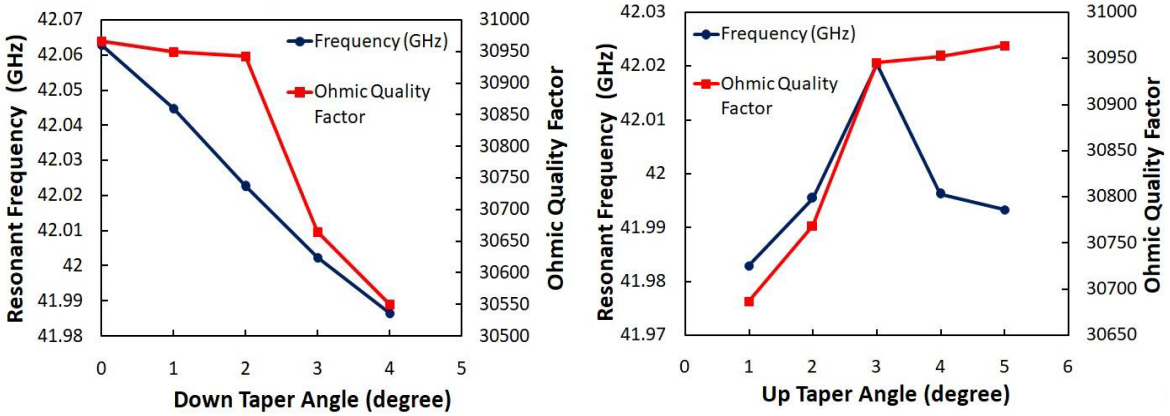

Figure 9. Variation of resonant frequency and Ohmic quality factor with (a) input taper angle at output taper angle 3° and, (b) output taper angle at input taper angle 2°, ($L_{\text{down}} = 30\,\text{mm}$, $L_{\text{cavity}} = 44\,\text{mm}$, $L_{\text{up}} = 46\,\text{mm}$).

4.1.3. Variation of Taper Length

The resonant frequency and quality factor decrease with the increase in the length of the both input and output taper sections (Fig. 10). At 30 mm length of input taper section, the resonant frequency is around 42.0 GHz (Fig. 10(a)). For getting the resonant frequency of 42 GHz, it is better to keep the length of output taper section between 44 mm and 48 mm (Fig. 10(b)). The final design parameters of the present 42 GHz gyrotron are listed in Table 4.

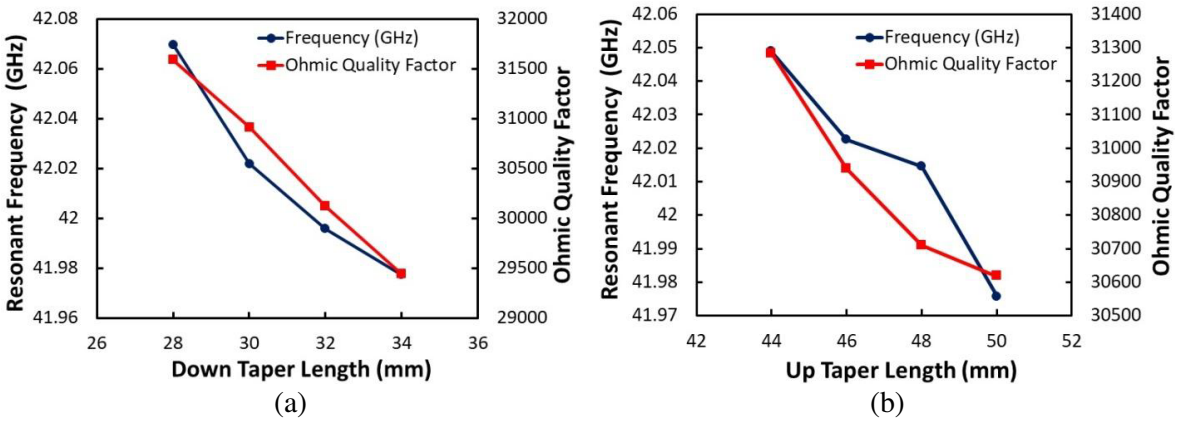

Figure 10. Variation of resonant frequency and Ohmic quality factor with (a) input taper length at $L_{\text{up}} = 46\,\text{mm}$ and, (b) output taper length at $L_{\text{down}} = 30\,\text{mm}$ ($L_{\text{cavity}} = 44\,\text{mm}$, $L_{\text{up}} = 46\,\text{mm}$, $\theta_{\text{down}} = 2^\circ$, $\theta_{\text{up}} = 3^\circ$).

Table 4. Design specifications of 42 GHz, 200 kW gyrotron.

Particulars	Specifications
Mode	TE_{03}
Beam voltage (V_b)	65 kV
Beam current (I_b)	10 A
Velocity ratio	1.4
Magnetic field	1.61 Tesla
Wall radius (r_w)	11.57 mm
Beam radius (r_b)	6.06 mm
Harmonic number (s)	1, i.e., fundamental mode
Output power	200 kW
Efficiency	35%
Wall loading	$<2.0\,\text{kW/cm}^2$
L/λ	6.3
Diffractive Q	860

4.2. Beam Present Simulation

In the beam present case, a gyrating electron beam is introduced at the input end of the tapered section to introduce oscillations inside the cavity using EMISSION command assigned with beam parameters as given in Table 4. With the beam radius 6.06 mm, electron beam is coupled to the second radial maximum of the operating TE_{031} mode in the resonator. The outer boundary of resonating structure is assumed to be a perfect conductor in the simulation. The axial component of the applied guiding magnetic field is constant along the interaction structure. The zero percent beam spreading is considered in the simulation. Sufficient numbers of beamlets have been taken to obtain accurate simulation results which depend on azimuthal resolution of the emitting surface. For the analysis of electron bunch and energy transfer phenomena, phase spaces for the momenta and positions of electrons are recorded at simulation time 150 ns.

In Fig. 11(a), the trajectory of all the electrons in the tapered cavity is shown which shows the minimum beam spreading. After zooming, the phase space of beamlets at the output port of the

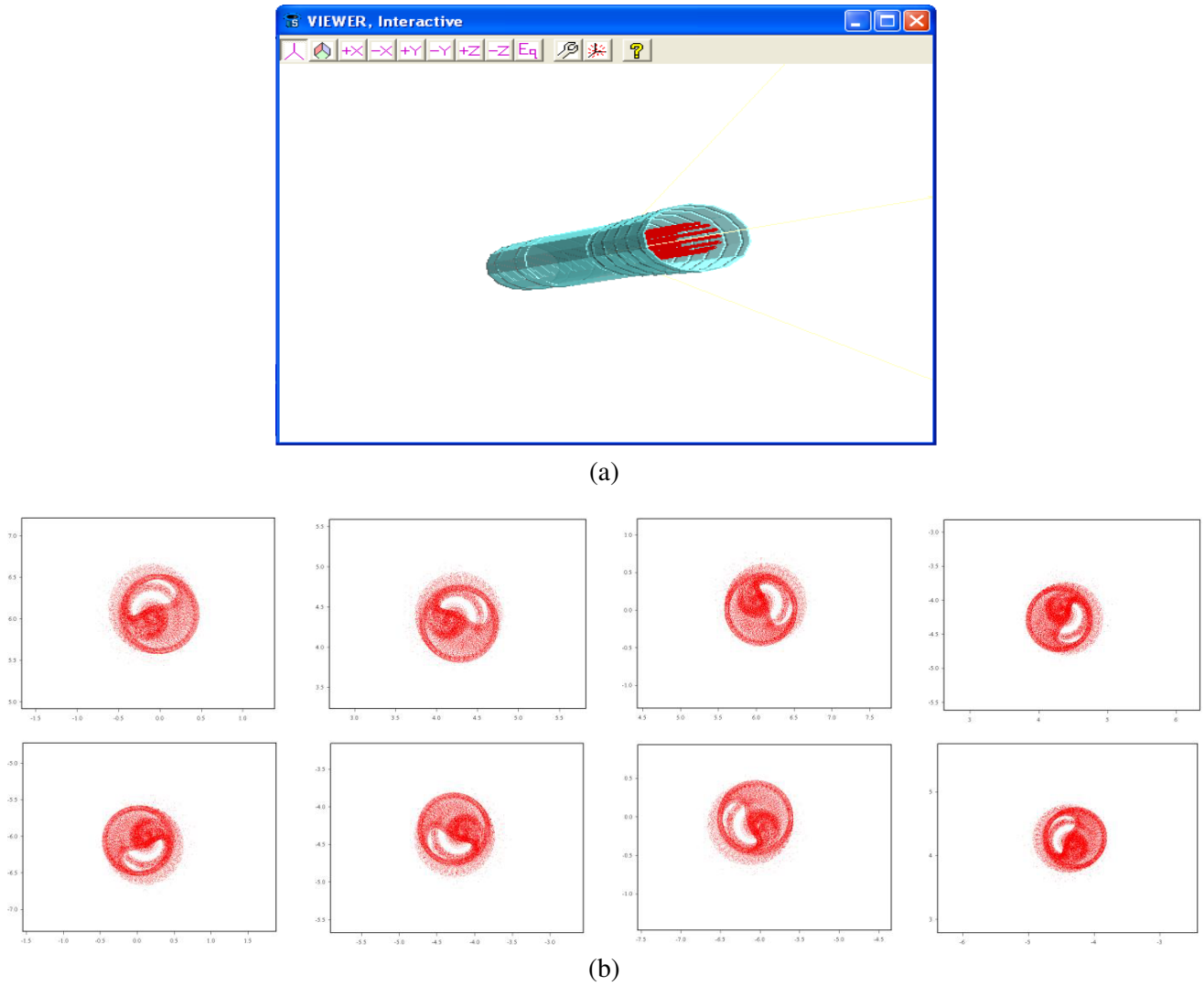

(a)

(b)

Figure 11. (a) Gyrating electron beam in the tapered interaction structure. (b) Phase space of particles in the all the beamlets observed at the end of simulation.

interaction structure at the end of simulation is shown in Fig. 11(b). Obviously, the bunching is formed in all the beamlets, and they all have constant phase relationship with each other. After the completion of the simulation run, absolute vector field profiles are observed at the output end of the cavity as shown in Fig. 12. This PIC code does not discriminate between the modes. If the mode observed in hot simulation is similar to the desired mode, it confirms the energy transfer in same electromagnetic mode. Simulation results obtained confirm the exact TE_{03} mode of operation of cavity in beam presence. To observe the frequency of operation in hot condition, the field is probed in time domain, and then its Fourier transform is done. The field is probed at the point location of maximum electric field in the straight section, and the frequency spectrum is obtained by applying Fourier transform of this field as shown in Fig. 13. The field demonstrates saturation after 100 ns, and it is characterized by a single-frequency component peaked at 42.022 GHz which supports the exact frequency of operation. The time monitored frequency of operation is also observed which shows that initially due to noise signals, device operates at several frequencies, but after 80 ns it is finally settled at 42 GHz of operation (Fig. 14(a)). Therefore, all these results clearly demonstrate the exact mode and frequency of operation of the interaction structure. The axial field profile value is the maximum in straight region as shown in Fig. 14(b). In down taper region, it is almost zeros while in up taper region it is oscillatory with

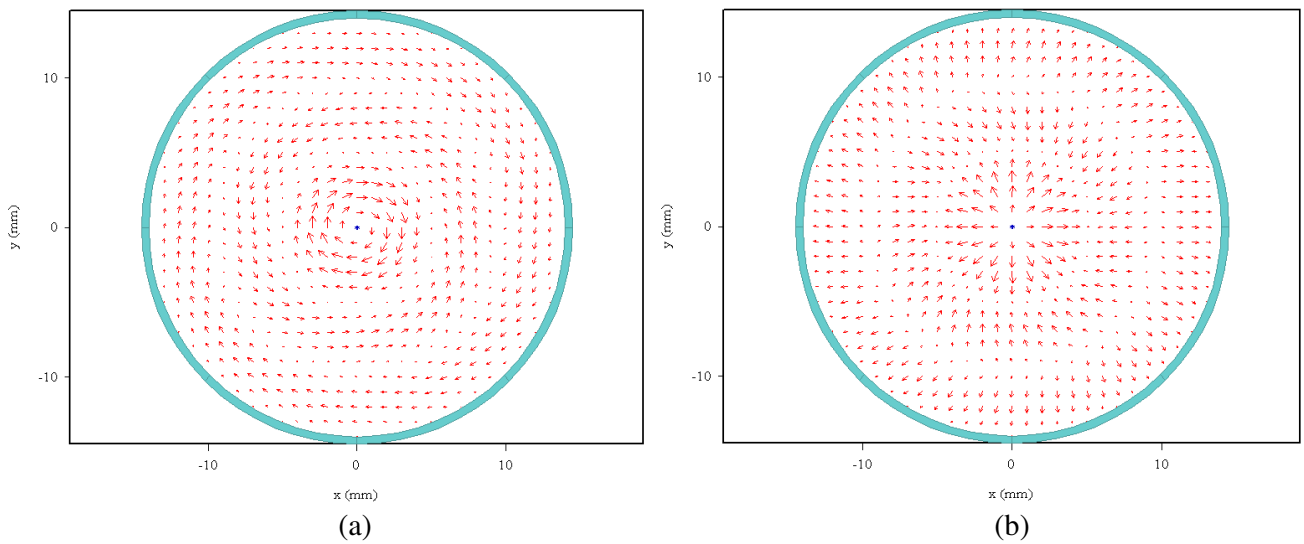

Figure 12. Vector plot of absolute field profiles (a) electric field and (b) magnetic field observed at the end of simulation at the output end of the cavity.

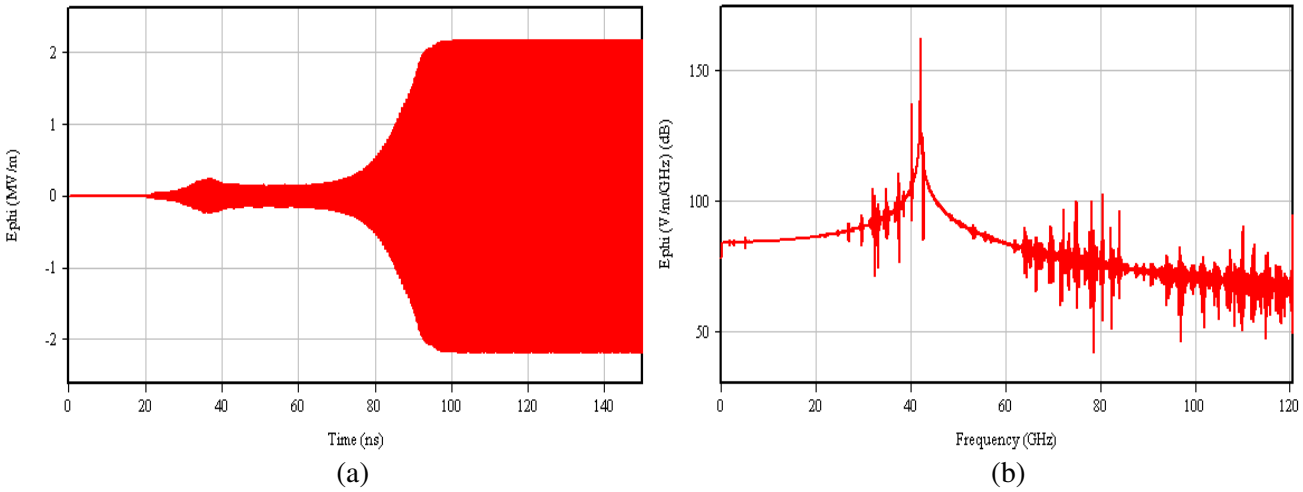

Figure 13. (a) Time domain variation of field values recorded in cavity and (b) its frequency spectra.

decreased magnitude.

In order to understand the interaction process, the phases of all the particles are monitored. The energy of all the particles is modulated as simulation proceeds continuously in time step by step (Fig. 15(a)). The overall result is a net transfer of energy from the beam to the cavity fields as a majority of the beam electrons become confined inside the initial gyration circle. The maximum number of particles have smaller energy than its initial value which represents a net transfer of energy from the electron beam to the RF fields. This can also be understood with the positive power of electrons as shown in Fig. 15(b), which decreases along the interaction positive power of all the particles is reduced, and hence the net energy transfer to RF takes place. In Figs. 15(c) and 15(d), normalized energy and phases of all electrons obtained through self-consistent single-mode (SSM) analysis [16] are shown which also demonstrates an energy transfer from electron beam to RF along the axial length of cavity in a similar way to that obtained from PIC simulation in Fig. 15(a).

From the simulation, the growth of RF output power is observed as shown in Fig. 16(a). Initially,

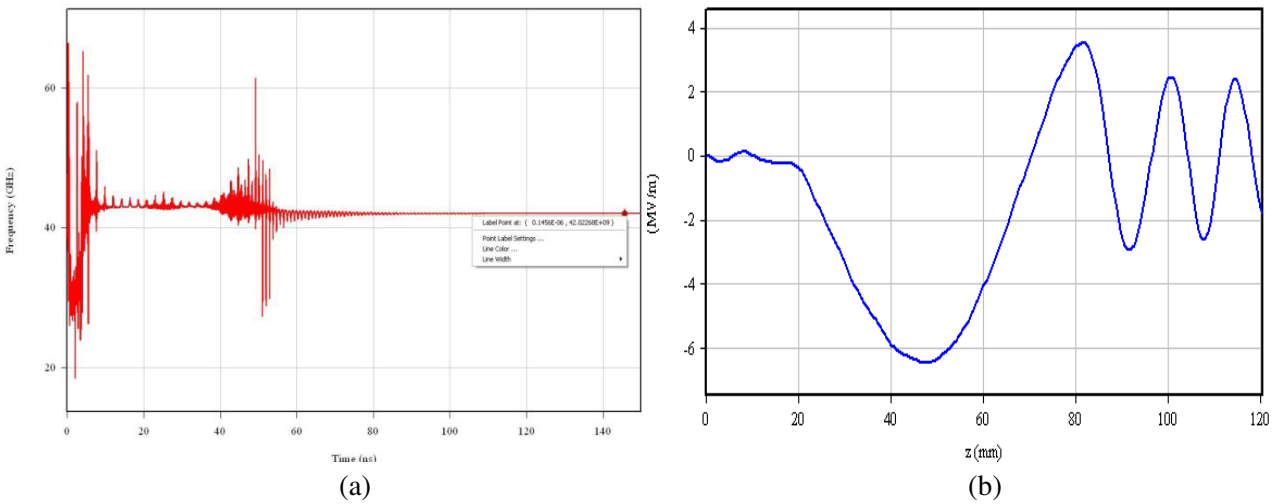

Figure 14. (a) Resonant frequency monitor in time frame and (b) axial electric field profile.

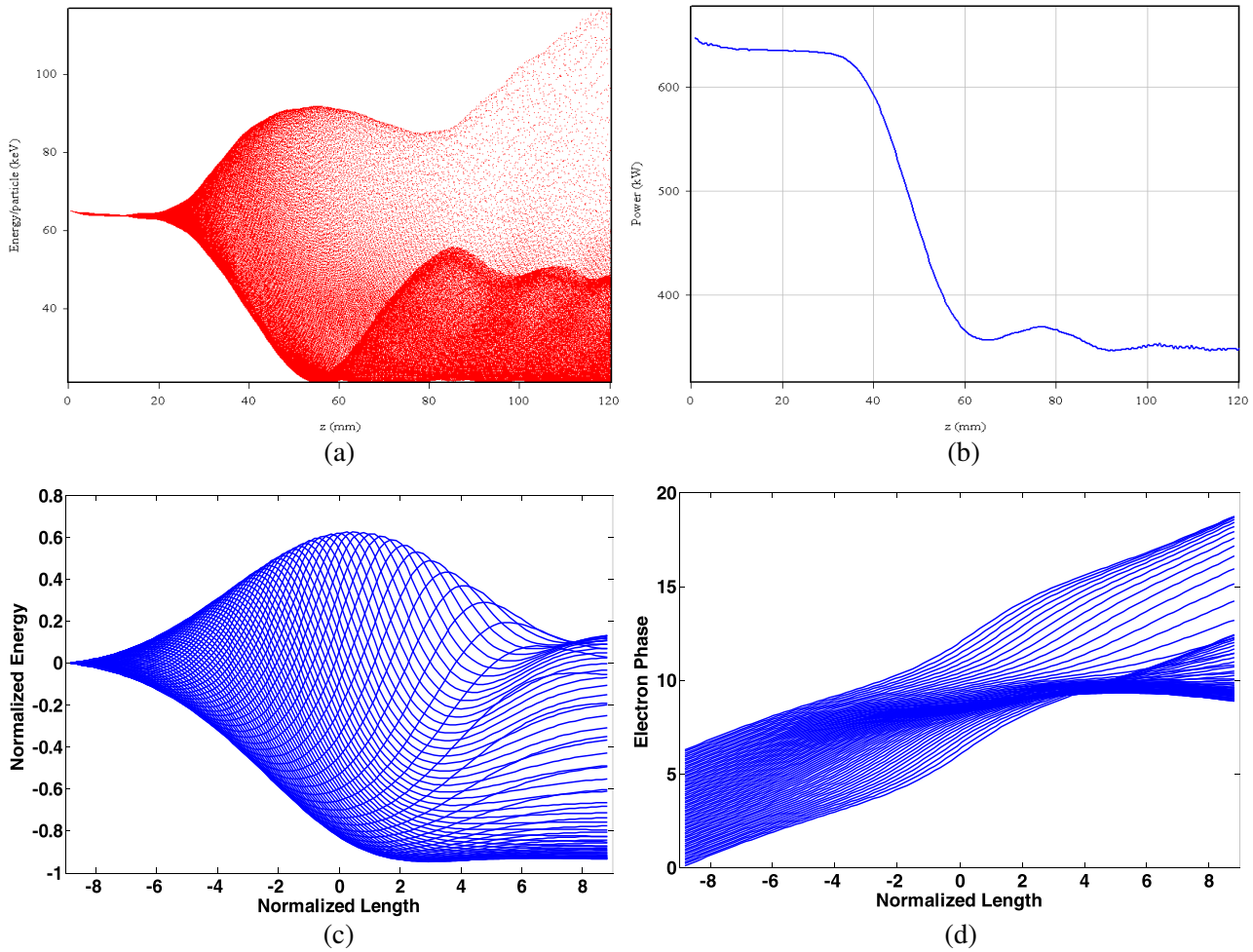

Figure 15. (a) Energy of all the particles along the interaction length and (b) electron positive energy variation along cavity axial distance at the end of PIC simulation. (c) Normalized energy and (d) phase (in radian) of all the electrons along the normalized interaction length from SSM analysis.

the power level is low and has large fluctuations. After some time, it reaches saturated value. Since the cavity takes some time to start operation in desired mode from the background of noise signal and at some time instance, once the desired EM field in TE_{03} mode is established in the cavity, it

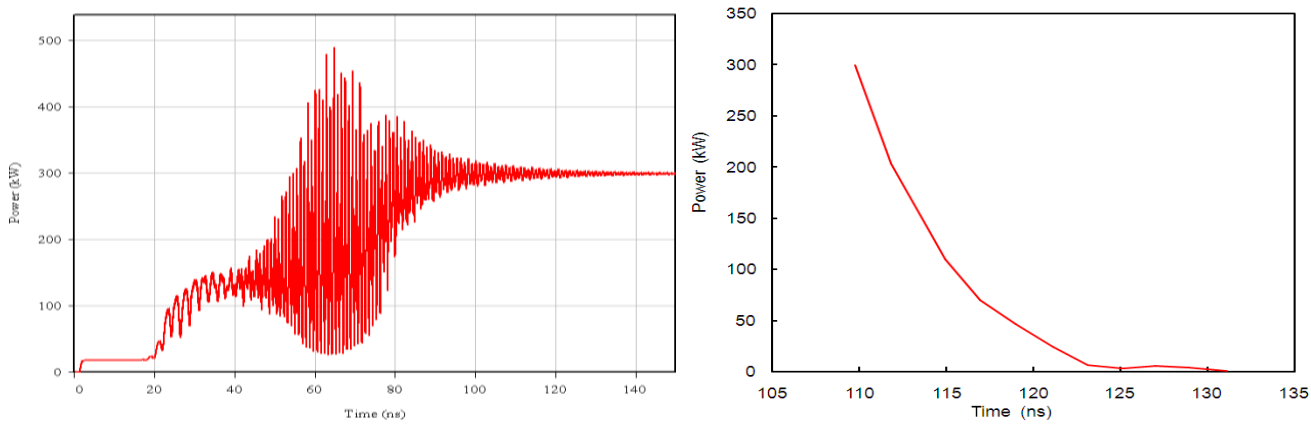

Figure 16. (a) Output power growth in time domain. (b) Exponential decay of power with time.

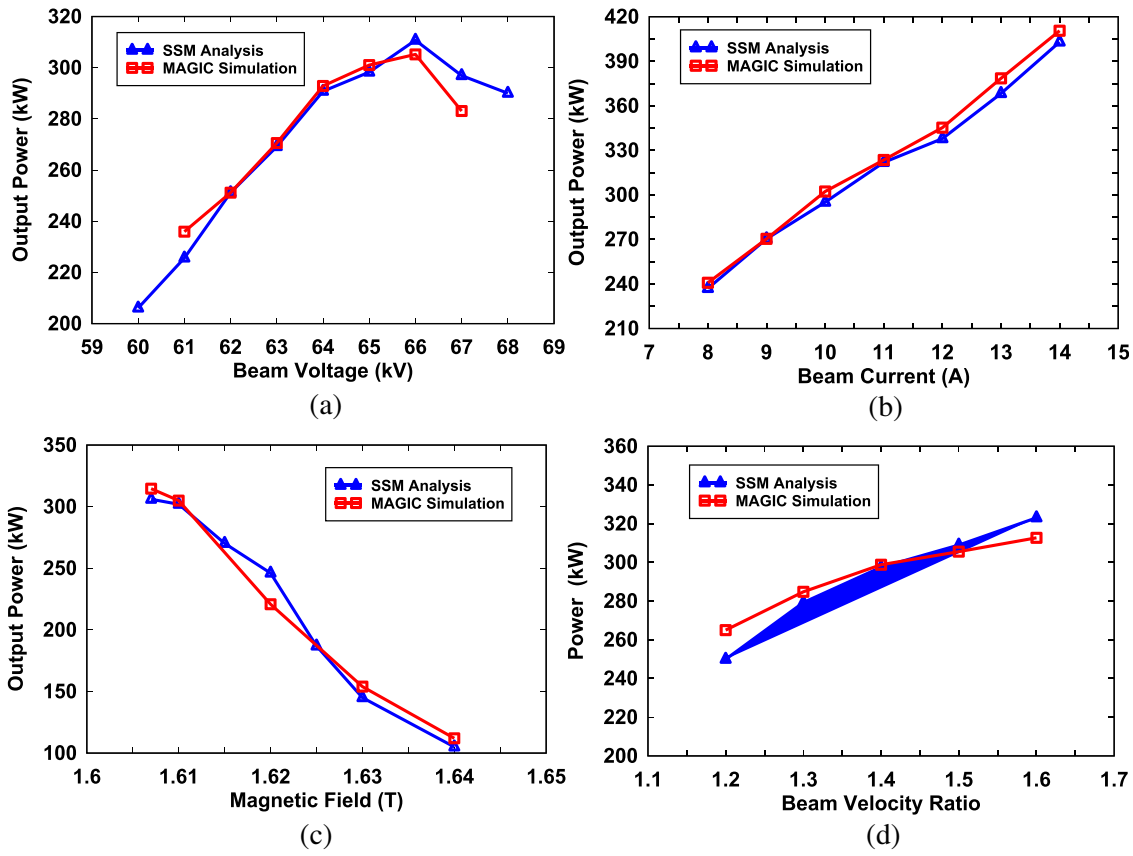

Figure 17. Output power variation with (a) beam voltage ($I_b = 10\,\text{A}$, $B_o = 1.61\,\text{T}$, $\alpha = 1.4$), (b) beam current ($V_b = 65\,\text{kV}$, $B_o = 1.61\,\text{T}$, $\alpha = 1.4$), (c) beam velocity ratio ($V_b = 65\,\text{kV}$, $I_b = 10\,\text{A}$, $B_o = 1.61\,\text{T}$), and (d) DC magnetic field ($V_b = 65\,\text{kV}$, $I_b = 10\,\text{A}$, $\alpha = 1.4$) for TE_{03} mode.

starts growing in the same mode and is finally saturated to give a stable continuous output. From this figure, it is evident that the saturated output power is 300 kW after 100 ns with around 46% efficiency operating at 42 GHz with TE_{03} mode. The diffractive quality factor is also calculated to know the selectivity/strongness of that mode. The diffractive Q factor of the cavity has been calculated by the decay of output power after the current of beam has been deliberately turned off at a given time in steady state (Fig. 16(b)). The relaxation time τ of the decay process is then determined, and a calculation according to $Q = \omega\tau$ yields a Q factor of 859.55. The Q of the cavity must be predetermined, since the cavity Q determines the start oscillation threshold and the saturated output power.

4.3. Validation of Simulation Results

Using simulation, the calculations for output power are carried out with the parameters as beam energy, beam velocity ratio, beam current, and applied static magnetic field. The simulated results are compared with those obtained from the self-consistent single-mode analysis presented by Singh et al. [16]. These

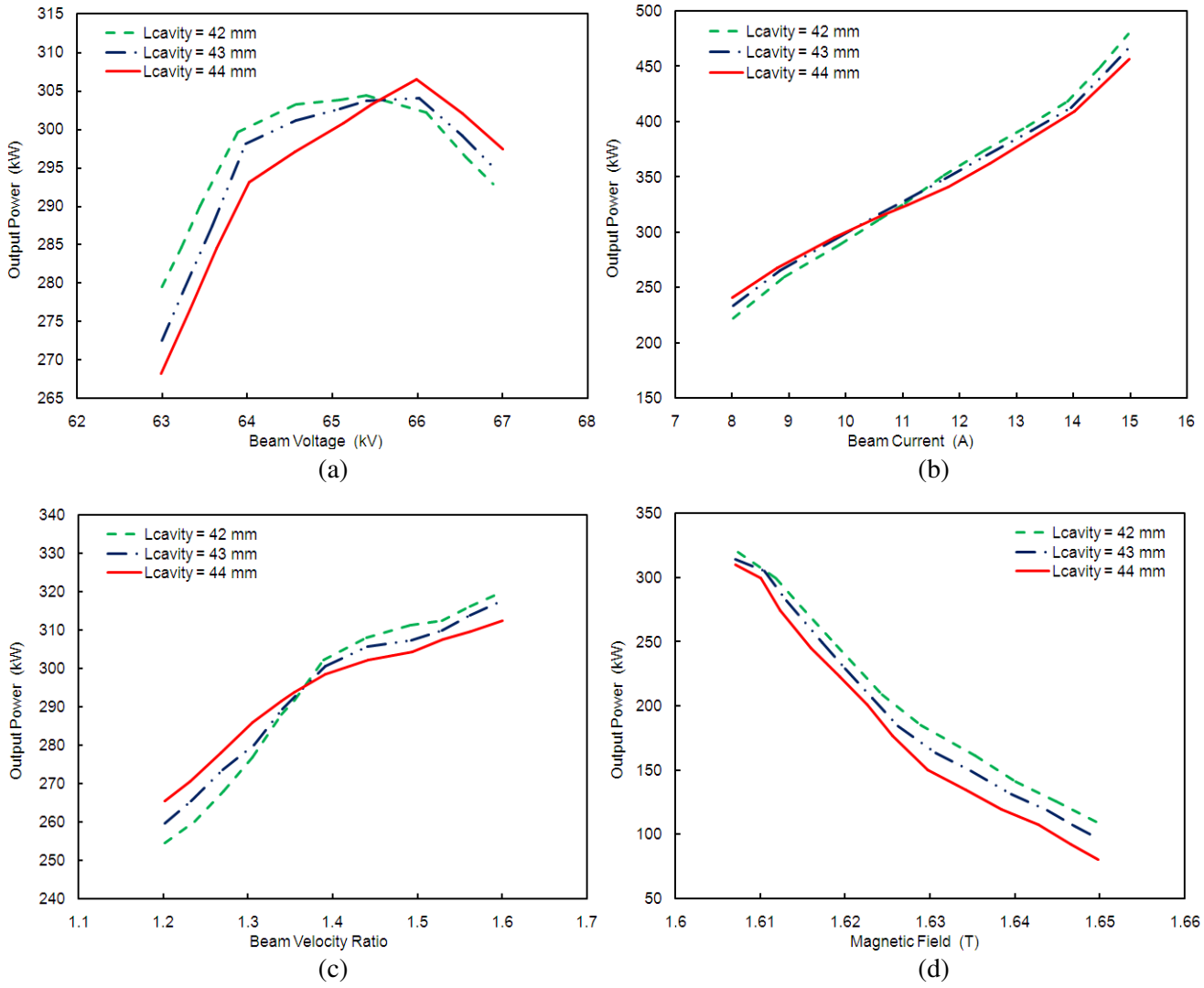

Figure 18. Output power variation as a function (a) beam voltage ($I_b = 10$ A, $B_o = 1.61$ T, $\alpha = 1.4$), (b) beam current ($V_b = 65$ kV, $B_o = 1.61$ T, $\alpha = 1.4$), (c) beam velocity ratio ($V_b = 65$ kV, $I_b = 10$ A, $B_o = 1.61$ T), and (d) DC magnetic field ($V_b = 65$ kV, $I_b = 10$ A, $\alpha = 1.4$) for different midsections length.

comparisons show close agreement of the results within 2% to 8% of difference (Fig. 17). With the increase of beam voltage, the output power decreases after attaining the maximum at 66 kV (Fig. 17(a)). With increasing the beam current, higher efficiency and output power can be achieved (Fig. 17(b)), but this often leads to the beam instability caused by the space charge effects in the adiabatic compression region of the electron beam. With the small increase in the magnetic field, the effects of space charge can be compensated which leads to restoring the higher efficiency [15]. With increasing the beam velocity ratio, the output power increases due to the increase in transverse component of beam velocity, and hence the increase in the energy transfer to RF takes place (Fig. 17(c)). With the detuning of magnetic field, a large degradation of output power is obtained as shown in Fig. 17(d). Hence, the applied magnetic field should be properly maintained along the interaction structure to achieve efficient performance. Simulations are also performed with beam energy, beam current, beam velocity ratio, and applied magnetic field to observe the sensitivity of the device operation on the performance in terms of output power for the axial length of cylindrical section as a parameter (Fig. 18). The three values of cylindrical straight section length are considered which are $L_{\text{cavity}} = 42.0\,\text{mm}$, 43.0 mm, and 44.0 mm. However, from the design goals, it is obvious that one can conveniently consider the cavity geometry corresponding to $L_2 = 44.0\,\text{mm}$ as the best choice to carry out the interaction computation, and the diffractive quality factor calculated is around 860. These figures explicitly demonstrate that for the design parameters given in Table 4, the output power is more than 250 kW with around 46% efficiency.

5. CONCLUSION

The detailed investigation of RF behavior of a 42 GHz conventional tapered cylindrical cavity gyrotron has been presented using PIC Code 'MAGIC'. PIC code used here is well suited for observing the beam-wave interaction behavior in the gyrotron oscillators over the other PIC codes for operating at millimeter to terahertz regime. Fully nonlinear behavior of the interaction mechanism in terms of saturation and efficiency of output radiation is demonstrated. The design of gyrotron is systematically presented to observe the beam-wave interaction phenomena in it. The beam absent and present cases have been considered for the investigation of device performance. Beam absent analysis presented ensures the device operation in the desired TE_{031} mode at 42 GHz resonant frequency using eigenmode solver. The electric and magnetic field patterns and their variations along radial as well as axial directions were also presented to ensure the exact TE_{03} mode of operation. The device interaction structure is optimized by observing the resonant frequency and Ohmic quality factor varying with different structure parameters. The calculation of diffractive quality factor using PIC code is discussed. In the beam present case, a gyrating electron beam is introduced at the left end of the confining interaction structure to drive the oscillations inside which the exact mode is finally set up in the cavity. Electric and magnetic field patterns obtained at the end of simulation also confirms the TE_{031} mode of device operation in the beam presence case. The maximum of field has been observed in the straight cylindrical section which is necessary for the maximum energy transfer during the beam-wave interaction. The axial particle distribution has been shown which reveals the minimum beam spreading. The frequency spectrum of the recoded field has a single peak at 42 GHz which shows that the device is strongly intended to operate at 42 GHz resonant frequency. Electron beamlets observed at the end of simulation show the explicit bunching mechanism of the particles. The energy distribution of all the particles along the interaction length has been observed which shows a net energy transfer from the electron beam to RF. The estimated total positive power of particles clearly supports the same. The output power growth has been estimated at the output end cross section of the interaction structure. Initially, the output power shows a varying nature, but after 80 ns, it saturates around 300 kW with around 46% efficiency in a stable manner. Output power has been calculated by varying the different structures as well as electron beam parameters such as beam energy, beam current, beam velocity ratio, and applied DC magnetic field with the mid-section length as a parameter. This shows that the designed parameters are capable of achieving the desired output power level above 250 kW. These results of output power have been compared with the analytical ones obtained through the self-consistent single-mode analysis and have been found in a close agreement. The design approach and PIC simulation presented here could be helpful in the design and analysis of future gyrotron oscillators operating at terahertz regime.

ACKNOWLEDGMENT

One of the authors (Ashutosh) is thankful to Center of Research in Microwave Tube, Department of Electronics Engineering, Indian Institute of Technology (BHU), Varanasi and Department of Electronics Engineering, National Institute of Technology, Patna for providing their valuable support.

REFERENCES

1. Thumm, M., "State-of-the-art of high-power gyro-devices and free electron masers," *Journal of Infrared, Millimeter, and Terahertz Waves*, Vol. 41, No. 1, 1–140, 2020.
2. Felch, K. L., B. G. Danly, H. R. Jory, K. E. Kreischer, W. Lawson, B. Levuson, and R. J. Temkin, "Characteristics and applications of fast-wave gyro-devices," *Proceedings of the IEEE*, Vol. 87, No. 5, 752–781, 1999.
3. Singh, U., N. Kumar, T. P. Singh, et al., "A review on the applications of high power, high frequency microwave source: Gyrotron," *J. Fusion Energy: Springer*, Vol. 30, 257–276, 2011.
4. Krier, L., I. Gr. Pagonakis, K. A. Avramidis, G. Gantenbein, S. Illy, J. Jelonnek, J. Jin, H. P. Laqua, A. Marek, D. Moseev, M. Thumm, and W7-X Team, "Theoretical investigation on possible operation of a 140 GHz 1 MW gyrotron at 175 GHz for CTS plasma diagnostics at W7-X," *Physics of Plasmas*, Vol. 27, 113107, 2020.
5. Kumar, A., N. Kumar, U. Singh, V. Vyas, and A. K. Sinha, "RF behavior and cavity design for 0.3 THz, 4 kW gyrotron for material processing application," *Infrared Physics & Technology*, Vol. 55, No. 4, 337–344, 2012.
6. Baja, V. S., M. K. Hornstein, K. E. Kreischer, J. R. Sirigir, P. P. Wosko, M. L. Mak-Jurkauska, J. Herzfel, R. J. Temki, and R. G. Griffin, "250 GHz CW gyrotron oscillator for dynamic nuclear polarization in biological solid state NMR," *Journal of Magnetic Resonance*, Vol. 189, 251–279, 2007.
7. Edgcombe, C. J., *Gyrotron Oscillators — Their Principles and Practice*, Taylor and Francis, London, 1993.
8. McDermott, D. B., N. C. Luhmann, Jr., D. S. Furuno, A. Kupiszewski, and H. R. Jory, "Operation of a millimeter-wave harmonic gyrotron," *J. of Infrared Milli. Waves*, Vol. 4, No. 4, 639–664, 1983.
9. Danly, B. G. and R. J. Temkin, "Generalized nonlinear harmonic gyrotron theory," *Phys. Fluids*, Vol. 29, 561–567, 1986.
10. Geng, Z., R. Zhang, X. Yan, Y. Liao, and S. Xu, "Design and simulation of a W-band gyrotron oscillator based on self-consistent nonlinear theory," *Microw. Opt. Technol. Lett.*, Vol. 62, 3175–3179, 2020.
11. Singh, A. and P. K. Jain, "RF behavior of a 35 GHz conventional cavity gyrotron using multimode analysis and PIC simulation," *Journal of Electromagnetic Waves and Application*, Vol. 35, No. 18, 2428–2446, 2021, doi: 10.1080/0920507.2021.1952655.
12. Singh, U., U. Goswami, H. Khatun, N. Kumar, N. Shekhawat, A. Kumar, V. Yadav, M. K. Sharma, A. Mishra, S. K. Sharma, M. K. Alaria, A. Bera, R. R. Rao, and A. K. Sinha, "P3-1: Design of 42 GHz, 200 kW gyrotron," *2010 IEEE International Vacuum Electronics Conference (IVEC)*, 331–332, 2010, doi: 1.1109/IVELE.2010.5503414.
13. Kartikeyan, M. V., A. Kumar, S. Kamakshi, P. K. Jain, S. Illy, E. Borie, B. Piosczyk, and M. K. Thumm, "RF-behavior of a 200 kW, CW gyrotron," *IEEE Trans. Plasma Science*, Vol. 20, No. 3, 631–636, June 2008.
14. Ludeking, L., *Manual of MAGIC Tool Suite*, ATK Mission Research Corporation, 2007.
15. Kreischer, K. E., B. G. Danly, J. B. Schutkeker, and R. J. Temkin, "The design of megawatt gyrotrons," *IEEE Trans. Plasma Science*, Vol. 13, No. 6, December 1985.
16. Singh, A., B. Ravi Chandra, and P. K. Jain, "Multimode behavior of a 42 GHz, 200 kW gyrotron," *Progress In Electromagnetics Research B*, Vol. 42, 75–91, 2012.